Cell Reports
Physical Science

CellPress
OPEN ACCESS

Article

Room Temperature Formation of Semiconductor Grade α-$FAPbI_3$ Films for Efficient Perovskite Solar Cells

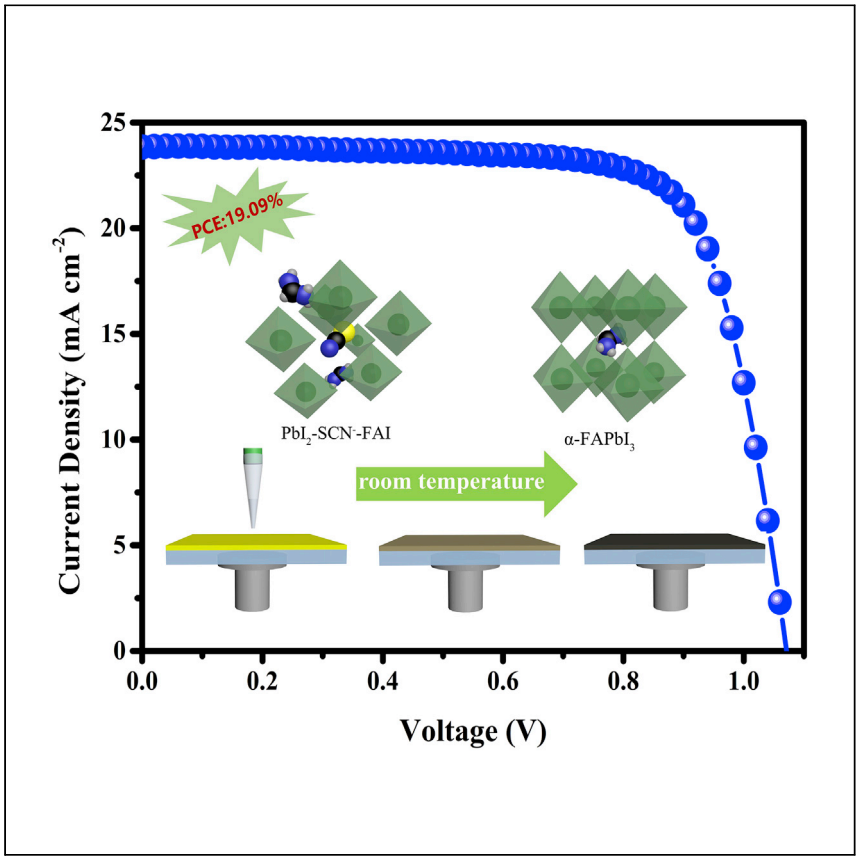

α-$FAPbI_3$ is a front-runner perovskite material for highly efficient solar cells, although its preparation typically requires high-temperature annealing. Chen et al. report a facile method for fabricating high-quality α-$FAPbI_3$ films at room temperature and reveal the mechanism of the formation of α-$FAPbI_3$ through theoretical and experimental methods.

Zhiliang Chen, Hengkai Zhang, Fang Yao, Chen Tao, Guojia Fang, Gang Li

gjfang@whu.edu.cn (G.F.)
gang.w.li@polyu.edu.hk (G.L.)

HIGHLIGHTS

Method for fabricating α-$FAPbI_3$ at room temperature

Mechanism of the formation of α-$FAPbI_3$ at room temperature

Highly efficient room temperature perovskite solar cells

Unique trend of PCE evolution in stability test

Chen et al., Cell Reports Physical Science 1, 100205
September 23, 2020 © 2020 The Authors.
https://doi.org/10.1016/j.xcrp.2020.100205

Cell Reports
Physical Science

CellPress
OPEN ACCESS

Article

Room Temperature Formation of Semiconductor Grade α-$FAPbI_3$ Films for Efficient Perovskite Solar Cells

Zhiliang Chen,[1,2] Hengkai Zhang,[1] Fang Yao,[2] Chen Tao,[2] Guojia Fang,[2,*] and Gang Li[1,3,*]

SUMMARY

Formamidinium lead iodide ($FAPbI_3$) perovskite is a front-runner material for efficient perovskite solar cells (PSCs) due to its high light-absorption coefficient, narrow band gap, and superior photostability and thermostability. High-quality $FAPbI_3$ perovskite formation typically requires an >160°C annealing process to induce phase transition from the photoinactive yellow phase (δ-$FAPbI_3$) to the photoactive black phase (α-$FAPbI_3$). However, this high-temperature annealing can induce defects in the films and hinders application in flexible solar cells. Here, we report a facile method to fabricate high-quality α-$FAPbI_3$ perovskite films at room temperature, without thermal annealing or vacuum-assisted processes. Combined computational and experimental results reveal the crystallization mechanism of α-$FAPbI_3$ formation at room temperature. We demonstrate PSCs with a power-conversion efficiency of 19.09%, which is the highest efficiency for room temperature PSCs to the best of our knowledge. This study may offer a cost-effective way to fabricate highly efficient PSCs at room temperature.

INTRODUCTION

Organic-inorganic hybrid perovskite solar cells (PSCs) have been developing rapidly over the last decade thanks to the low material and fabrication cost and high power-conversion efficiency (PCE). Since the first report in 2009, the PCE of PSCs has risen dramatically, from 3.8% to 25.2%,[1–7] rivaling that of the commercialized silicon-based solar cells. To date, PSCs with PCEs of >22% mainly use formamidinium lead iodide ($FAPbI_3$)-dominated perovskite as a light absorber due to their superior opto-electrical properties[8–11]—narrower band gap, longer charge-diffusion length, and better photostability and thermostability.[12–16] However, when preparing the $FAPbI_3$-based perovskite films, high-temperature annealing is indispensable to induce phase transition from the photoinactive yellow phase (δ-$FAPbI_3$) to the photoactive black phase (α-$FAPbI_3$).[17] Such annealing is incompatible with the common low-cost plastic substrates such as poly(ethylene terephthalate) (PET) and poly(ethylene 2,6-naphthalate) (PEN). The high-temperature annealing process increases the fabrication cost and extends the energy payback time for photovoltaics, which will hinder the commercialization of this photovoltaic technique. Recently, efforts have been made to lower the annealing temperature of $FAPbI_3$ perovskite. For instance, incorporating other cations (methylammonium [MA], Cs) to develop mix-cation perovskite has been proven to be an effective approach to prepare high-performance PSCs with lower annealing temperatures.[18–26] In addition, $FAPbI_3$-dominated mixed-phase perovskite systems ($(FAPbI_3)_x(MAPbBr_3)_{1-x}$) have been widely studied due to its facile preparation at lower temperatures and good phase stability.[27–30] However, the band gaps of these mixed-phase perovskite systems become larger (1.58–1.62 eV), close to or larger than that of the primary perovskite $MAPbI_3$, which

[1]Department of Electronic and Information Engineering, Research Institute for Smart Energy (RISE), The Hong Kong Polytechnic University, Hong Kong SAR, 999077, P.R. China

[2]Key Laboratory of Artificial Micro- and Nano-structures of Ministry of Education of China, School of Physics and Technology, Wuhan University, Wuhan 430072, P.R. China

[3]Lead Contact

*Correspondence: gjfang@whu.edu.cn (G.F.), gang.w.li@polyu.edu.hk (G.L.)

https://doi.org/10.1016/j.xcrp.2020.100205

This is an open access article under the CC BY-NC-ND license (http://creativecommons.org/licenses/by-nc-nd/4.0/).

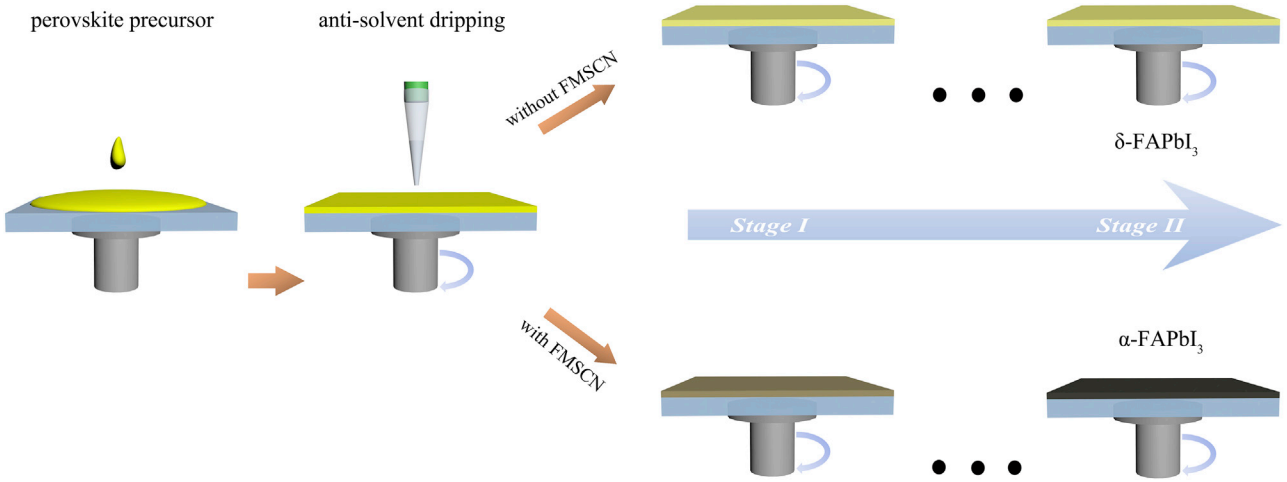

Figure 1. Schematic Illustration of Fabrication of $FAPbI_3$-Based Perovskite Films
The experimental procedure of fabricating α-$FAPbI_3$ perovskite films at room temperature using a facile spin-coating method.

is unprofitable for developing highly efficient PSCs with narrow band-gap perovskite. Therefore, forming narrow band-gap perovskites at low temperatures for highly efficient PSCs is desirable for pushing the commercialization of this promising photovoltaic technology.

In the present work, we develop a facile method for fabricating high-quality α-$FAPbI_3$ perovskite films at much lower temperatures (i.e., room temperature), free from any thermal annealing or vacuum-assisted processes. Specifically, FMSCN (formamidinium thiocyanate [FASCN] and methylammonium thiocyanate [MASCN] in an optimal molar ratio) are introduced into the perovskite precursor solution to form the formamidinium iodide (FAI)-SCN^--PbI_2 intermediate phase, which can convert to α-$FAPbI_3$ perovskite at room temperature. Computational and experimental results clarify the crystallization mechanism of α-$FAPbI_3$ at room temperature. Applying this strategy, we demonstrate room temperature PSCs with an efficiency of 19.09%. As far as we know, this is the best result reported to date for room temperature-processed PSCs[31–37] (see Table S1).

RESULTS AND DISCUSSION

Fabrication and Characterization of Room Temperature Formed α-$FAPbI_3$ Films

The facile fabrication method for α-$FAPbI_3$ perovskite film formation at room temperature is illustrated in Figure 1. The precursor solution with or without FMSCN was first spin coated onto the substrate/ITO (tin-doped indium oxide)/SnO_2. During the antisolvent process, the film from the precursor solution containing FMSCN gradually turned to dark brown with time, while the film from the pristine precursor solution (without FMSCN) remained light yellow even after a long spin.

The optical images of the resultant films from the precursor solution containing different amounts of FMSCN (0, 10, 20, 30, 50, and 70 mol%) are shown in Figure 2A. The film presented smoother and darker as the content of FMSCN in precursor solution increased, suggesting a gradual crystallization of black-phase perovskite in the films. This was confirmed by the X-ray powder diffraction (XRD) patterns in Figure 2B. For convenience, the composition $FAPbI_3$+x mol% FMSCN (see

CellPress
OPEN ACCESS

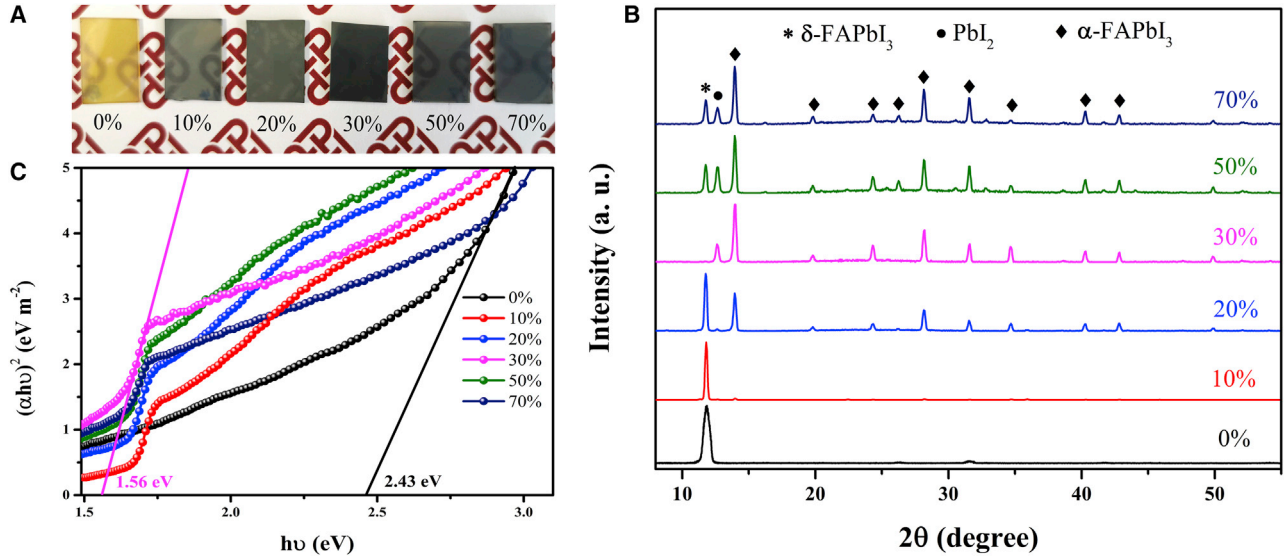

Figure 2. Characterization of the Room Temperature Films

(A) Photographs, (B) XRD patterns, and (C) Tauc plots of room temperature formed perovskite films prepared from precursor solution containing different amounts of FMSCN.

Experimental Procedures) is abbreviated as x-FMS throughout the article, in which x is the molar percentage of FMSCN in the precursor solution and FMS represents FMSCN. 0-FMS means perovskite precursor solution without FMSCN. The 0-FMS film exhibited strong diffraction peaks at ~11.8°, indicating the formation of yellow phase (δ-phase) perovskite in the film,[38] which is considered not applicable for photovoltaic devices. When 10 mol% FMSCN was added, the 11.8° diffraction peak relatively diminished and became narrower compared to the 0-FMS sample. Meanwhile, weaker peaks at 13.95°, 19.85°, 24.3°, 28.15°, 31.55°, 34.7°, 40.3°, and 42.85° emerge, indicating the formation of cubic phase α-$FAPbI_3$ in the film.[39,40] When the content of FMSCN increased to an appropriate level (30 mol %), the 11.8° peak disappeared, and the film exhibited α-$FAPbI_3$ perovskite phase, suggesting that highly crystalized α-$FAPbI_3$ perovskite films were formed without any annealing treatment. However, further increasing the content of FMSCN to higher levels (50 and 70 mol%), the 11.8° peak emerges again, indicating the phase instability of the films when excess FMSCN was incorporated in the precursor solution. The ultraviolet (UV)-visible absorption spectra of the 0-FMS and 30-FMS films are shown in Figure S1. The band gaps of all room temperature formed perovskite films using Tauc analysis are depicted in Figure 2C and Table S2. The band gap decreased from 2.43 (δ-$FAPbI_3$) to 1.56 eV (α-$FAPbI_3$) when the content of FMSCN increased from 0 to 30 mol%, and slightly increased to 1.58 eV (α-$FAPbI_3$-δ-$FAPbI_3$ mix) when the content of FMSCN further increased to 70 mol%, which are in line with the optical images and XRD results above.

Mechanism of Formation of α-$FAPbI_3$ at Room Temperature

Adding an appropriate amount of FMSCN in the precursor solution can result in highly crystalized α-$FAPbI_3$ perovskite film at room temperature. As the FMSCN incorporation lies in the center of the phenomenon, the key point in this perovskite-formation process is expected to be the strong affinity of SCN^-, PbI_6^{4-}, and FA^+. In the conventional precursor solution with *N*,*N*-dimethylformamide (DMF) and dimethyl sulfoxide (DMSO) as the solvent, the PbI_2-DMSO-FAI intermediate

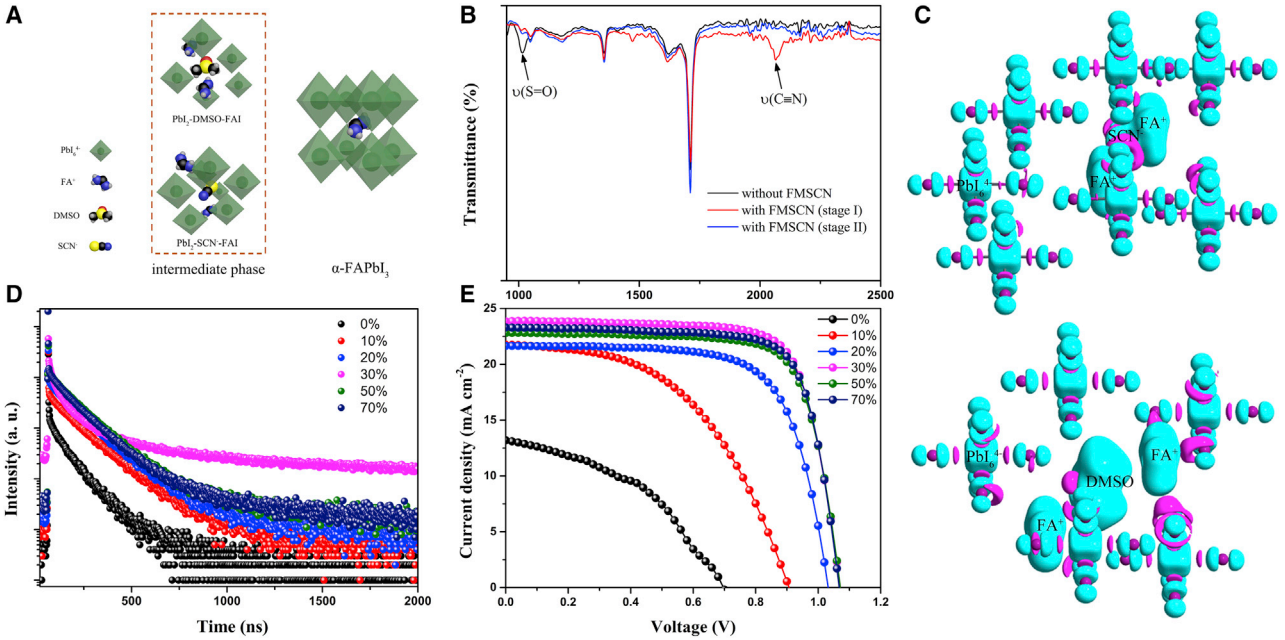

Figure 3. Schematic Illustration and Characterization of the Room Temperature Perovskite Film and Corresponding Photovoltaic Devices

(A) The schematic illustration of the formation of α-$FAPbI_3$ from different intermediate phases.

(B) FTIR spectra of the perovskite films on KBr substrates.

(C) Electron difference density for PbI_2-SCN^--FAI (top) and PbI_2-SCN^--FAI (bottom). Isosurfaces are set at 0.018|e|/Å3. Magenta and cyan regions denote the electrons obtained and lost, respectively.

(D and E) TRPL spectra of perovskite films on glass (D) and *J-V* curves of PSCs (E) based on a precursor solution containing different amounts of FMSCN.

phase exists in the precursor film-drying process, which then converts to perovskite film after annealing.[41] We speculated that compared to DMSO, SCN^- has a stronger interaction with PbI_6^{4-} and FA^+. When SCN^- is in the precursor solution, there is the PbI_2-SCN^--FAI intermediate phase instead of the PbI_2-DMSO-FAI. After the antisolvent dripping, SCN^- is easily released from the spinning film in the form of HSCN due to the unstable property of this adduct[37,42]; then, the PbI_2-SCN^--FAI intermediate phase converts to α-$FAPbI_3$ perovskite at room temperature. For the conventional perovskite-formation process, since the boiling point of DMSO is relatively high, the thermal annealing process is necessary to remove DMSO so that the PbI_2-DMSO-FAI intermediate phase can convert to the resultant $FAPbI_3$ perovskite.[41] The mechanism discussed above is illustrated in Figure 3A.

Fourier transform infrared spectroscopy (FTIR) was performed to verify the proposed hypothesis. Figure 3B shows the FTIR results of different samples. It can be observed that the precursor film without FMSCN exhibits a characteristic peak at ~1,012 cm^{-1}, which stems from the stretching vibration of S=O in the FAI-DMSO-PbI_2 complex.[43] When 30 mol% FMSCN is incorporated, the precursor film, which is formed immediately after the antisolvent dripping (stage I), exhibits a strong vibration peak at 2,061 cm^{-1}, which belongs to the stretching vibration of C≡N in SCN^-. Meanwhile, the stretching vibration at 1,012 cm^{-1} that belongs to the S=O almost disappears,[44] which indicates the stronger interaction of SCN^- with PbI_2 and FAI than DMSO. When the precursor film is further spun for a certain time (stage II), the C≡N vibration also disappears, implying that the SCN^- is released from the precursor film during the spinning. The energy-dispersive X-ray spectroscopy (EDS) in Figure S2 shows that only a little S (0.33 mass%) is present in the resultant film, confirming that most of the SCN^- is released from the 30 mol% FMSCN-incorporated film.

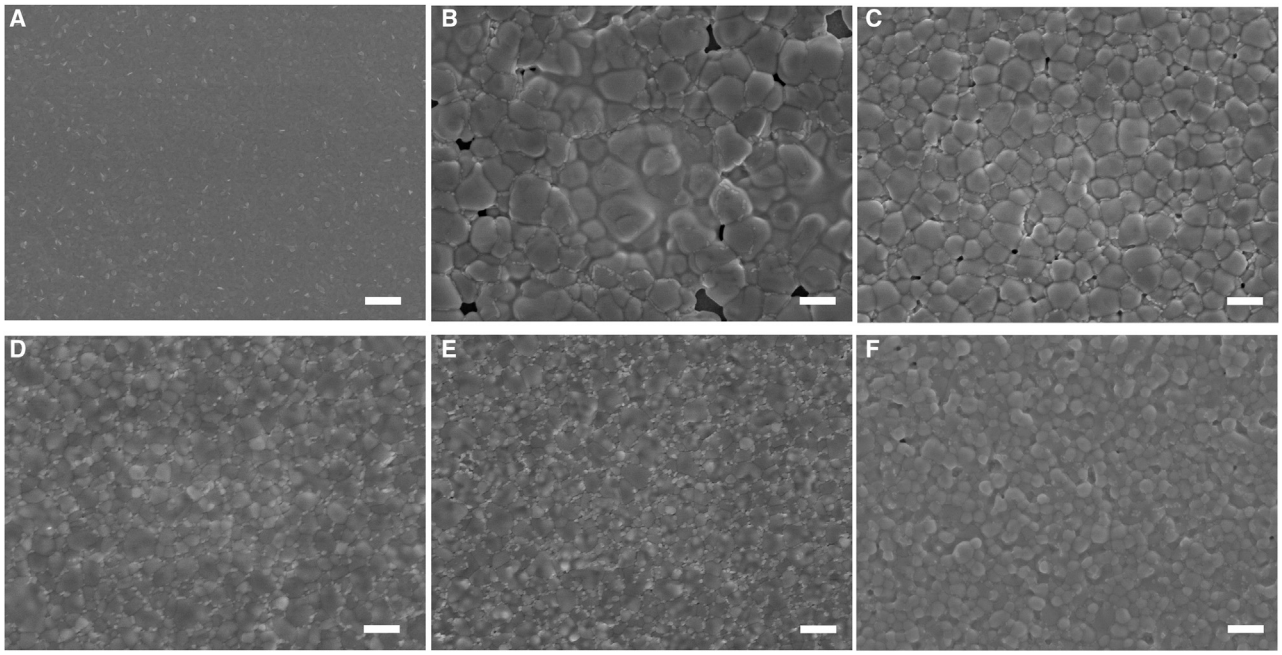

Figure 4. Scanning Electron Microscopy (SEM) Images of Room Temperature Perovskite Film

(A–F) SEM images of room temperature deposited perovskite films prepared from precursor solution (A) without and with (B) 10 mol%, (C) 20 mol%, (D) 30 mol%, (E) 50 mol%, and (F) 70 mol% FMSCN. Scale bar, 1 μm.

The relative interaction of SCN^- and DMSO with PbI_2 and FAI was further investigated using density functional theory (DFT) based on the first principle. The electron difference density of the proposed model was carried out in Atomistix ToolKit (ATK) code, and the results are presented in Figure 3C, where magenta and cyan regions denote the obtained and lost electrons, respectively. As we can see, the charge density of SCN^- and FA^+ was connected (Figure 3C, top) to each other, suggesting that mass electron transfer occurs between the SCN^- and FA^+, which confirms the strong interaction between SCN^- and FA^+. However, the case of DMSO and FA^+ is different from that of SCN^- and FA^+; the charge densities of DMSO and FA^+ are isolated (Figure 3C, bottom), suggesting less electron transfer between DMSO and FA^+. These results provide solid evidence that SCN^- exhibits much stronger interaction with FAI than with DMSO.

Effect of the Content of FMSCN on the Perovskite Films and Solar Cells

Time-resolved photoluminescence (TRPL) measurement was performed to investigate the impact of the content of FMSCN in precursor solution on the charge carrier dynamics of the room temperature formed perovskite films. The TRPL decay curves of the perovskite films on glass are shown in Figure 3E and the bi-exponential function fitted parameters are presented in Table S3. In this case, the short lifetime τ_1 was dominated by bimolecular recombination, while the long lifetime τ_2 was dominated by trap-assisted recombination.[45–47] The 30-FMS film exhibits longer τ_2 than the 0-, 10-, and 20-FMS samples, implying less charge recombination in the perovskite film, which agrees with the compact and pinhole-free morphology of the 30-FMS films that are of higher quality and have fewer defects (Figure 4D). The 50- and 70-FMS films exhibit decreased τ_2 lifetimes compared to the 30-FMS film, which indicates that excess FMSCN would result in more trap states in the perovskite films, leading to charge recombination and degrading the performance of the prepared photovoltaic devices.

To verify the applicability of the room temperature-processed perovskite in photovoltaic devices, a series of PSCs were fabricated using a planar configuration of ITO/SnO_2/perovskite/Spiro-OMeTAD/Au. It was found that the proportion of FASCN in FMSCN could be neither too high nor too low to fabricate high-performance PSCs (Figure S3; Table S4). Adding moderate FASCN was conducive to efficiency improvement, but excess FASCN would dramatically decrease the performance of the devices. We optimized the molar ratio of MASCN and FASCN, fixing it to 8.8:1.2 before further optimization of the content of FMSCN. The representative *J-V* curves of PSCs prepared from the precursor solution with a different content of FMSCN are depicted in Figure 3F, and the corresponding photovoltaic parameters are summarized in Table S5. All of the photovoltaic parameters, especially short-circuit current density (J_{SC}) and fill factor (FF), are greatly improved when increasing the content of FMSCN to 30 mol%. These improvements could stem from the suppression of δ-$FAPbI_3$ and the formation of α-$FAPbI_3$ in the perovskite films, respectively, which can facilitate light absorption and hence, photogenerated charge carriers in PSCs. In addition, the pinhole-free and compact morphology of the perovskite films (30 mol%) can reduce the charge recombination, contributing to the improved open circuit voltage (V_{OC}) and FF. However, when excess FMSCN (50 mol%, 70 mol%) was incorporated in the precursor solution, J_{SC}, FF, and V_{OC} of the resultant devices simultaneously decreased moderately, which may be due to the re-appearance of δ-$FAPbI_3$ (Figure 2B) and the morphologies of the perovskite films (Figures 4E and 4F).

Performance of the Champion Devices

An ultra-thin interlayer of butylamine hydrobromide-2-phenylethylamine hydroiodide (BABr-PEAI) complex was introduced between the perovskite and Spiro-OMeTAD layers to improve the performance of the room temperature PSCs (Figure 5A). After carefully optimizing the experimental process, we achieved high PCEs of 19.09% (19.04%) with a V_{OC} of 1.07 V (1.07 V), a J_{SC} of 23.84 mA cm^{-2} (23.4 mA cm^{-2}), and a FF of 0.74 (0.76) under reverse (forward) scan directions for the best-performing room temperature PSCs (Figure 5B). The incident photon-to-current conversion efficiency (IPCE) spectrum and integrated J_{SC} curve of the corresponding device was plotted in Figure 5C, which shows a photocurrent onset at 835 nm. The band gap (1.56 eV) calculated from the IPCE spectrum is consistent with the value obtained from the absorption spectrum (Figure S4). The integrated J_{SC} (22.83 mA cm^{-2}) from the IPCE spectrum matches well with that extracted from the *J-V* curves, showing a very slight 3% mismatch with the mean value of J_{SC} under reverse and forward scan directions, which confirms the reliability of the measurement results. The IPCE spectra of PSCs with different contents of FMSCN were plotted in Figure S5. It can be seen that the onsets of the IPCE spectra, which correspond to the band gaps of the perovskite film, showed the same shift trend as the results in Figure 2C. We performed a thermal stress test to examine the stability of the room temperature PSCs, in which the epoxy-sealed devices were put on an 85°C hot plate, covered with an opaque Petri dish to keep out the light, and tested periodically. The temporal evolution of the PCEs is shown in Figure 5D. In the thermal stress test, poly[bis(4-phenyl)(2,4,6-trimethylphenyl)amine] (PTAA) was used instead of Spiro-OMeTAD to focus on the perovskite stability,[5,48,49] and the *J-V* curves are shown in Figure S6. Unlike the evolution trends in other works that the PCE dropped drastically in the first several hours and then decreased gradually,[5,50] the PCE here showed a slight increase and remained constant at the beginning (within 8 h) of 85°C heating, followed by a ~10% "burn-in" drop until 24 h. The PSC became relatively stable under thermal stress, slightly decreasing from 90% to 83% of its initial efficiency after ~265 h of thermal stress test in this stage. We speculate that the thermal stress test has an

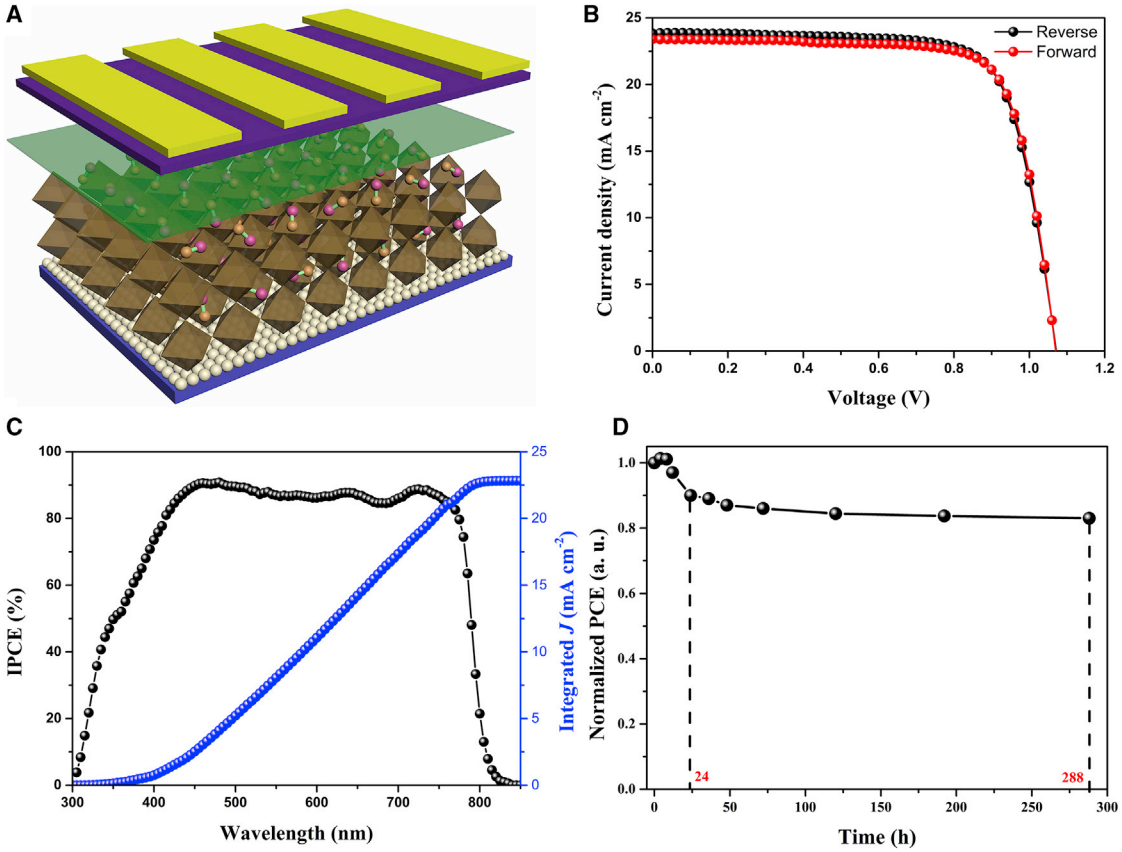

Figure 5. Photovoltaic Performance of Room Temperature α-$FAPbI_3$ Perovskite-Based PSCs

(A) Schematic structure of the champion device. From top to bottom are Au, Spiro-OMeTAD, BABr-PEAI, perovskite, SnO_2 quantum dots (QDs), and ITO.

(B) *J-V* curves of the champion device measured under reverse and forward scan directions.

(C) IPCE spectrum and the integrated current density curve of the best-performing devices.

(D) The thermal stability test results of one epoxy-sealed device, in which Spiro-OMeTAD was replaced by PTAA for thermal testing and BABr-PEAI complex interlayer was absent.

influence on the PSCs in two aspects: one is the thermal modification of the room temperature formed perovskite film, the other is the thermal decomposition of the whole PSCs. For the former, the thermal annealing would lead to increased perovskite grain size and hence improved performance of the PSCs. This improvement is finite and will reach the limit when the perovskite layer achieved an optimal status. However, the decomposition of the functional layers of the PSC, including perovskite layer, hole transport layer, and Au back contact, under thermal stress is continuous as time goes by. In the early stage, the thermal modification played a major part in the two aspects, so the PCE of the devices slightly increased. When the thermal modification reached the limit and the thermal decomposition dominated, the PCE then showed a burn-in drop. This unique temporal evolution trend of the PCEs at the early stage of thermal stress test is related to a compromise of the thermal "healing" modification of the perovskite films and the thermal decomposition of the solar cells. We transferred room temperature formed perovskite films to a hot plate for annealing at 100°C for 1 h. The perovskite film exhibited increased grain size, improved crystallinity, and the same compact morphology after annealing (Figures S7 and S8), which would lead to fewer grain boundaries and hence a decreased possibility of charge recombination in the perovskite film, resulting in higher performance of the PSCs. The devices based on annealed perovskite films showed slightly

increased performance (mainly FF and PCE) compared to the room temperature formed PSCs (Figure S9), which is consistent with the thermal stress result. These results may inspire research into increasing the lifetime of photovoltaic devices under thermal work conditions.

In summary, we developed a novel facile method for fabricating high-quality perovskite films at room temperature for efficient PSCs. Using FMSCN as a precursor additive, highly crystalized compact α-$FAPbI_3$ perovskite films can be obtained without any thermal annealing or vacuum-assisted processes. The room temperature crystallization mechanism is clarified by computational and experimental results. Finally, we demonstrate room temperature PSCs with efficiencies as high as 19.09%. To the best of our knowledge, this is the highest efficiency reported for room temperature PSCs. Our work offers an effective method for preparing high-performance PSCs at room temperature, which will favor the development of highly efficient and low-cost flexible photovoltaic devices.

EXPERIMENTAL PROCEDURES

Resource Availability

Lead Contact

For any information on this work, please communicate with the Lead Contact, Prof. Dr. Gang Li (gang.w.li@polyu.edu.hk).

Materials Availability

The authors did not produce any new kind of reagent in this work.

Data and Code Availability

The authors declare that the experimental data discussed in the work here can be found in the article and the Supplemental Information. All other data can be obtained from the Lead Contact upon reasonable request.

Materials

ITO glass substrates (8 Ω sq^{-1}) were purchased from Xiang Science & Technology. The SnO_2 nanoparticle (15% in H_2O colloidal dispersion) was purchased from Alfa Aesar. PbI_2 (99.99%, trace metals basis), MASCN (>97%), and FASCN (>97%) were purchased from TCI. $PbBr_2$ (99.999%, trace metals basis), bis(trifluoromethane) sulfonimide lithium salt (Li-TFSI) (99.95%, trace metals basis), 4-tert-butylpyridine (tBP) (98%), DMF (anhydrous, 99.8%), DMSO (anhydrous, ≥99.9%), acetonitrile (anhydrous, 99.8%), 2-propanol (anhydrous, 99.5%), toluene (anhydrous, 99.8%), and chlorobenzene (anhydrous, 99.8%) were purchased from Sigma-Aldrich. FAI, methylammonium bromide (MABr), BABr, and PEAI were purchased from Greatcell Solar Materials Pty. Spiro-OMeTAD (99.5%) was purchased from Advanced Election Technology. PTAA was purchased from Xi'an Polymer Light Technology, and Au was purchased from Chow Sang Sang Jewelry. All of the materials were used as received.

Device Fabrication

The ITO glasses were cleaned using a standard operating procedure. Specifically, the ITO glasses were sonicated with hot detergent and then scrubbed with a dust-free cloth, followed by sonication with deionized water, acetone, and isopropyl alcohol, respectively, for 15 min. The cleaned ITO glasses were dried by nitrogen flow and then treated with UV-ozone for 20 min before the deposition of electron transporting layers (ETLs). The SnO_2 colloid solution was diluted with deionized water and spin coated onto the substrates at 4,000 rpm for 30 s. Then, the substrates

were annealed at 150°C for 30 min. Before the deposition of the perovskite layer, the substrates were treated with UV-ozone again for 15 min to obtain a better surface-wetting property. A total of 1.4 M $FAPbI_3$, 0.14 M PbI_2, and 0.07 M $MAPbBr_3$ were dissolved in a mixture of DMF and DMSO (8:1, v:v). Then, different amounts (0–70 mol%) of FMSCN (FASCN and MASCN in 1.2:8.8, mol:mol) were added to obtain the final perovskite precursor solution. For the deposition of the perovskite layer, the filtered solution was dripped on the ITO/SnO_2 substrates, followed by a spin-coating process of 1,000 rpm for 5 s and 5,000 rpm for 120 s. After the high-speed process started for 10 s, 150 μL Coomassie Blue (CB) was dripped quickly on the center of the substrates. The obtained brilliant black perovskite film was kept in a dry box for at least 6 h to obtain a dry film. The BABr-PEAI complex precursor solution was prepared by mixing BABr solution (3 mg mL^{-1} in isopropyl alcohol [IPA]) and PEAI solution (5 mg mL^{-1} in IPA) with a volume ratio of 1:1 and then spin coated onto the perovskite surface at 5,000 rpm for 30 s. The substrates should be held 30 min before the deposition of the hole transport layer to obtain better surface wetting. The hole transporting layer was deposited by spin coating the Spiro-OMeTAD solution (72.3 mg mL^{-1} in chlorobenzene) with 28.8 μL tBP and 17.5 μL Li-TFSI solution (520 mg mL^{-1} in acetonitrile) onto the perovskite film at 3,000 rpm for 30 s. For the device thermal stability test, the PTAA layer was deposited by spin coating the PTAA solution (10 mg mL^{-1} in toluene) with 2 μL tBP and 2 μL Li-TFSI solution (520 mg mL^{-1} in acetonitrile) onto the perovskite film at 4,000 rpm for 30 s. The device was finished by thermal evaporating 80 nm Au as back contact. The active area was 4 mm^2.

Characterizations and Measurements

The XRD patterns were collected with a Rigaku SmartLab X-ray diffractometer. The FTIR measurement was performed on a Perkin-Elmer 2000 FTIR spectrometer. TRPL spectra were obtained by using an Edinburgh FLSP920 spectrophotometer installed with the excitation source of a 485-nm pulsed laser. The absorption spectra of the perovskite films were measured using a UV-visible spectrophotometer (CARY5000, Varian). The performance of the solar cells was tested using an Enlitech measurement system with a SUN 2000 solar simulator equipped with an AM 1.5 filter at 100 mW cm^{-2}. The IPCE spectrum was measured in air using a QE-R3011 system. The morphologies of PSCs were investigated using a high-resolution field emission scanning electron microscope (JEOL JSM-6335F).

SUPPLEMENTAL INFORMATION

Supplemental Information can be found online at https://doi.org/10.1016/j.xcrp.2020.100205.

ACKNOWLEDGMENTS

This work was financially supported by the Research Grants Council of Hong Kong (GRF grant 15246816 and CRF grant C5037-18G), the Project of Strategic Importance (project code 1-ZE29) and the Sir Sze-yuen Chung Endowed Professorship fund provided by the Hong Kong Polytechnic University, the Shenzhen Science and Technology Innovation Commission (project no. JCYJ20170413154602102), the National Natural Science Foundation of China (11674252), Special Funds for the Development of Strategic Emerging Industries in Shenzhen (JCYJ20170818113036217), the Science and Technology Department of Hubei Province (2019AAA020), and the Fundamental Research Funds for the Central Universities (2042019kf0317). Z.C. thanks Dr. Wei Yu for helping with the experiments and for valuable discussions.

AUTHOR CONTRIBUTIONS

Z.C., G.F., and G.L. designed all of the experiments. Z.C. fabricated and performed the main characterization of thin films and solar cells. H.Z. synthesized the SnO_2 nanoparticles and measured the stabilized PCE. F.Y. performed the EDS and IPCE measurements. Z.C. drafted the manuscript, guided by G.L. C.T. and G.L. assisted in revising the manuscript. G.F. and G.L. supervised the whole project.

DECLARATION OF INTERESTS

The authors declare no competing interests.

Received: April 21, 2020
Revised: July 19, 2020
Accepted: August 21, 2020
Published: September 23, 2020

REFERENCES

1. Kojima, A., Teshima, K., Shirai, Y., and Miyasaka, T. (2009). Organometal halide perovskites as visible-light sensitizers for photovoltaic cells. J. Am. Chem. Soc. *131*, 6050–6051.

2. Kim, H.S., Lee, C.R., Im, J.H., Lee, K.B., Moehl, T., Marchioro, A., Moon, S.J., Humphry-Baker, R., Yum, J.H., Moser, J.E., et al. (2012). Lead iodide perovskite sensitized all-solid-state submicron thin film mesoscopic solar cell with efficiency exceeding 9%. Sci. Rep. *2*, 591.

3. Zhu, Z., Zhao, D., Chueh, C.-C., Shi, X., Li, Z., and Jen, A.K.Y. (2017). Highly Efficient and Stable Perovskite Solar Cells Enabled by All-Crosslinked Charge-Transporting Layers. Joule *2*, 168–183.

4. Zhou, H., Chen, Q., Li, G., Luo, S., Song, T.-B., Duan, H.-S., Hong, Z., You, J., Liu, Y., and Yang, Y. (2014). Photovoltaics. Interface engineering of highly efficient perovskite solar cells. Science *345*, 542–546.

5. Jiang, Q., Zhao, Y., Zhang, X., Yang, X., Chen, Y., Chu, Z., Ye, Q., Li, X., Yin, Z., and You, J. (2019). Surface Passivation of Perovskite Film for Efficient Solar Cells. Nat. Photonics *13*, 460–466.

6. Kim, M., Kim, G.-H., Lee, T.K., Choi, I.W., Choi, H.W., Jo, Y., Yoon, Y.J., Kim, J.W., Lee, J., Huh, D., et al. (2019). Methylammonium Chloride Induces Intermediate Phase Stabilization for Efficient Perovskite Solar Cells. Joule *3*, 2179–2192.

7. National Renewable Energy Laboratory. Best research-cell efficiencies. https://www.nrel.gov/pv/assets/pdfs/best-research-cell-efficiencies.20191106.pdf.

8. Jiang, Q., Zhang, L., Wang, H., Yang, X., Meng, J., Liu, H., Yin, Z., Wu, J., Zhang, X., and You, J. (2016). Enhanced Electron Extraction Using SnO_2 for High-Efficiency Planar-Structure $HC(NH_2)_2PbI_3$-Based Perovskite Solar Cells. Nat. Energy *2*, 16177.

9. Jiang, Q., Chu, Z., Wang, P., Yang, X., Liu, H., Wang, Y., Yin, Z., Wu, J., Zhang, X., and You, J. (2017). Planar-Structure Perovskite Solar Cells with Efficiency beyond 21. Adv. Mater. *29*, 1703852.

10. Jeon, N.J., Na, H., Jung, E.H., Yang, T.-Y., Lee, Y.G., Kim, G., Shin, H.-W., Seok, S.I., Lee, J., and Seo, J. (2018). A Fluorene-Terminated Hole-Transporting Material for Highly Efficient and Stable Perovskite Solar Cells. Nat. Energy *3*, 682–689.

11. Yang, G., Zhang, H., Li, G., and Fang, G. (2019). Stabilizer-Assisted Growth of Formamdinium-Based Perovskites for Highly Efficient and Stable Planar Solar Cells with over 22% Efficiency. Nano Energy *63*, 103835.

12. Eperon, G.E., Stranks, S.D., Menelaou, C., Johnston, M.B., Herz, L.M., and Snaith, H.J. (2014). Formamidinium Lead Trihalide: A Broadly Tunable Perovskite for Efficient Planar Heterojunction Solar Cells. Energy Environ. Sci. *7*, 982.

13. Lee, J.W., Seol, D.J., Cho, A.N., and Park, N.G. (2014). High-efficiency perovskite solar cells based on the black polymorph of $HC(NH_2)_2PbI_3$. Adv. Mater. *26*, 4991–4998.

14. Xue, J., Lee, J.-W., Dai, Z., Wang, R., Nuryyeva, S., Liao, M.E., Chang, S.-Y., Meng, L., Meng, D., Sun, P., et al. (2018). Surface Ligand Management for Stable $FAPbI_3$ Perovskite Quantum Dot Solar Cells. Joule *2*, 1866–1878.

15. Min, H., Kim, M., Lee, S.U., Kim, H., Kim, G., Choi, K., Lee, J.H., and Seok, S.I. (2019). Efficient, stable solar cells by using inherent bandgap of α-phase formamidinium lead iodide. Science *366*, 749–753.

16. Juarez-Perez, E.J., Hawash, Z., Raga, S.R., Ono, L.K., and Qi, Y. (2016). Thermal Degradation of $CH_3NH_3PbI_3$ Perovskite into NH_3 and CH_3I Gases Observed by Coupled Thermogravimetry-Mass Spectrometry Analysis. Energy Environ. Sci. *9*, 3406–3410.

17. Yi, C., Luo, J., Meloni, S., Boziki, A., Ashari-Astani, N., Grätzel, C., Zakeeruddin, S.M., Röthlisberger, U., and Grätzel, M. (2016). Entropic Stabilization of Mixed A-Cation ABX_3 Metal Halide Perovskites for High Performance Perovskite Solar Cells. Energy Environ. Sci. *9*, 656–662.

18. Saliba, M., Matsui, T., Seo, J.Y., Domanski, K., Correa-Baena, J.P., Nazeeruddin, M.K., Zakeeruddin, S.M., Tress, W., Abate, A., Hagfeldt, A., and Grätzel, M. (2016). Cesium-containing triple cation perovskite solar cells: improved stability, reproducibility and high efficiency. Energy Environ. Sci. *9*, 1989–1997.

19. Chen, Z., Zheng, X., Yao, F., Ma, J., Tao, C., and Fang, G. (2018). Methylammonium, Formamidinium and Ethylenediamine Mixed Triple-Cation Perovskite Solar Cells with High Efficiency and Remarkable Stability. J. Mater. Chem. A Mater. Energy Sustain. *6*, 17625–17632.

20. Tu, Y., Yang, X., Su, R., Luo, D., Cao, Y., Zhao, L., Liu, T., Yang, W., Zhang, Y., Xu, Z., et al. (2018). Diboron-Assisted Interfacial Defect Control Strategy for Highly Efficient Planar Perovskite Solar Cells. Adv. Mater. *30*, e1805085.

21. Qin, P.L., Yang, G., Ren, Z.W., Cheung, S.H., So, S.K., Chen, L., Hao, J., Hou, J., and Li, G. (2018). Stable and Efficient Organo-Metal Halide Hybrid Perovskite Solar Cells via π-Conjugated Lewis Base Polymer Induced Trap Passivation and Charge Extraction. Adv. Mater. *30*, e1706126.

22. Dang, H.X., Wang, K., Ghasemi, M., Tang, M.C., Bastiani, M.D., Aydin, E., Dauzon, E., Barrit, E., Peng, J., Smilgies, D.-M., et al. (2019). Multi-Cation Synergy Suppresses Phase Segregation in Mixed-Halide Perovskites. Joule *3*, 1746–1764.

23. Wang, Y., Wu, T., Barbaud, J., Kong, W., Cui, D., Chen, H., Yang, X., and Han, L. (2019). Stabilizing heterostructures of soft perovskite semiconductors. Science *365*, 687–691.

24. Qin, P., Wu, T., Wang, Z., Zheng, X., Yu, X., Fang, G., and Li, G. (2019). Vitrification Transformation of Poly(Ethylene Oxide) Activating Interface Passivation for High-Efficiency Perovskite Solar Cells. Sol. RRL *3*, 1900134.

25. Yang, G., Qin, P., Fang, G., and Li, G. (2018). A Lewis Base-Assisted Passivation Strategy Towards Highly Efficient and Stable Perovskite Solar Cells. Sol. RRL *2*, 1800055.

26. Qin, P., Zhang, J., Yang, G., Yu, X., and Li, G. (2019). Potassium-Intercalated Rubrene as A Dual-Functional Passivation Agent for High

Efficiency Perovskite Solar Cells. J. Mater. Chem. A Mater. Energy Sustain. *7*, 1824–1834.

27. Jeon, N.J., Noh, J.H., Yang, W.S., Kim, Y.C., Ryu, S., Seo, J., and Seok, S.I. (2015). Compositional engineering of perovskite materials for high-performance solar cells. Nature *517*, 476–480.

28. Correa Baena, J.P., Steier, L., Tress, W., Saliba, M., Neutzner, S., Matsui, T., Giordano, F., Jacobsson, T.J., Srimath Kandada, A.R., Zakeeruddin, S.M., et al. (2015). Highly Efficient Planar Perovskite Solar Cells through Band Alignment Engineering. Energy Environ. Sci. *8*, 2928–2934.

29. Bi, D., Yi, C., Luo, J., Décoppet, J.-D., Zhang, F., Zakeeruddin, Shaik, M., Li, X., Hagfeldt, A., and Grätzel, M. (2016). Polymer-Templated Nucleation and Crystal Growth of Perovskite Films for Solar Cells with Efficiency Greater than 21%. Nat. Energy *1*, 16142.

30. Zhang, J., Wu, S., Liu, T., Zhu, Z., and Jen, A.K.Y. (2019). Boosting Photovoltaic Performance for Lead Halide Perovskites Solar Cells with BF_4- Anion Substitutions. Adv. Funct. Mater. *29*, 1808833.

31. Chen, Y., Zhao, Y., and Liang, Z. (2015). Non-Thermal Annealing Fabrication of Efficient Planar Perovskite Solar Cells with Inclusion of NH_4Cl. Chem. Mater. *27*, 1448–1451.

32. Zheng, X., Chen, B., Wu, C., and Priya, S. (2015). Room Temperature Fabrication of $CH_3NH_3PbBr_3$ by Anti-Solvent Assisted Crystallization Approach for Perovskite Solar Cells with Fast Response and Small J-V Hysteresis. Nano Energy *17*, 269–278.

33. Zhou, Y., Yang, M., Wu, W., Vasiliev, A.L., Zhu, K., and Padture, N.P. (2015). Room-Temperature Crystallization of Hybrid-Perovskite Thin Films via Solvent-Solvent Extraction for High-Performance Solar Cells. J. Mater. Chem. A Mater. Energy Sustain. *3*, 8178–8184.

34. Yin, M., Xie, F., Chen, H., Yang, X., Ye, F., Bi, E., Wu, Y., Cai, M., and Han, L. (2016). Annealing-Free Perovskite Films by Instant Crystallization for Efficient Solar Cells. J. Mater. Chem. A Mater. Energy Sustain. *4*, 8548–8553.

35. Pan, J., Mu, C., Li, Q., Li, W., Ma, D., and Xu, D. (2016). Room-Temperature, Hydrochloride-Assisted, One-Step Deposition for Highly Efficient and Air-Stable Perovskite Solar Cells. Adv. Mater. *28*, 8309–8314.

36. Zhang, H., Cheng, J., Li, D., Lin, F., Mao, J., Liang, C., Jen, A.K., Grätzel, M., and Choy, W.C. (2017). Toward All Room-Temperature, Solution-Processed, High-Performance Planar Perovskite Solar Cells: A New Scheme of Pyridine-Promoted Perovskite Formation. Adv. Mater. *29*, 1604695.

37. Han, Q., Bai, Y., Liu, J., Du, K.-Z., Li, T., Ji, D., Zhou, Y., Cao, C., Shin, D., Ding, J., et al. (2017). Additive Engineering for High-Performance Room-Temperature-Processed Perovskite Absorbers with Micron-Size Grains and Microsecond-Range Carrier Lifetimes. Energy Environ. Sci. *10*, 2365–2371.

38. Han, Q., Bae, S.H., Sun, P., Hsieh, Y.T., Yang, Y.M., Rim, Y.S., Zhao, H., Chen, Q., Shi, W., Li, G., and Yang, Y. (2016). Single Crystal Formamidinium Lead Iodide ($FAPbI_3$): Insight into the Structural, Optical, and Electrical Properties. Adv. Mater. *28*, 2253–2258.

39. Saidaminov, M.I., Abdelhady, A.L., Maculan, G., and Bakr, O.M. (2015). Retrograde solubility of formamidinium and methylammonium lead halide perovskites enabling rapid single crystal growth. Chem. Commun. (Camb.) *51*, 17658–17661.

40. Weller, M.T., Weber, O.J., Frost, J.M., and Walsh, A. (2015). Cubic Perovskite Structure of Black Formamidinium Lead Iodide, α-$[HC(NH_2)_2]PbI_3$, at 298 K. J. Phys. Chem. Lett. *6*, 3209–3212.

41. Jeon, N.J., Noh, J.H., Kim, Y.C., Yang, W.S., Ryu, S., and Seok, S.I. (2014). Solvent engineering for high-performance inorganic-organic hybrid perovskite solar cells. Nat. Mater. *13*, 897–903.

42. Ke, W., Xiao, C., Wang, C., Saparov, B., Duan, H.S., Zhao, D., Xiao, Z., Schulz, P., Harvey, S.P., Liao, W., et al. (2016). Employing Lead Thiocyanate Additive to Reduce the Hysteresis and Boost the Fill Factor of Planar Perovskite Solar Cells. Adv. Mater. *28*, 5214–5221.

43. Zhang, W., Jiang, Y., Ding, Y., Zheng, M., Wu, S., Lu, X., Gao, X., Wang, Q., Zhou, G., Liu, J., et al. (2017). Solvent-Induced Textured Structure and Improved Crystallinity for High Performance Perovskite Solar Cells. Opt. Mater. Express *7*, 2150.

44. Lee, K.K., Park, K.H., Kwon, D., Choi, J.H., Son, H., Park, S., and Cho, M. (2011). Ion-pairing dynamics of Li^+ and SCN^- in dimethylformamide solution: chemical exchange two-dimensional infrared spectroscopy. J. Chem. Phys. *134*, 064506.

45. Stranks, S.D., Burlakov, V.M., Leijtens, T., Ball, J.M., Goriely, A., and Snaith, H.J. (2014). Recombination Kinetics in Organic-Inorganic Perovskites: Excitons, Free Charge, and Subgap States. Phys. Rev. Appl. *2*, 034007.

46. Pascoe, A.R., Yang, M., Kopidakis, N., Zhu, K., Reese, M.O., Rumbles, G., Fekete, M., Duffy, N.W., and Cheng, Y.-B. (2016). Planar versus Mesoscopic Perovskite Microstructures: The Influence of $CH_3NH_3PbI_3$ Morphology on Charge Transport and Recombination Dynamics. Nano Energy *22*, 439–452.

47. Ahmad, S., Fu, P., Yu, S., Yang, Q., Liu, X., Wang, X., Wang, X., Guo, X., and Li, C. (2019). Dion-Jacobson Phase 2D Layered Perovskites for Solar Cells with Ultrahigh Stability. Joule *3*, 794–806.

48. Saliba, M., Matsui, T., Domanski, K., Seo, J.Y., Ummadisingu, A., Zakeeruddin, S.M., Correa-Baena, J.-P., Tress, W.R., Abate, A., Hagfeldt, A., and Grätzel, M. (2016). Incorporation of rubidium cations into perovskite solar cells improves photovoltaic performance. Science *354*, 206–209.

49. Meng, L., Sun, C., Wang, R., Huang, W., Zhao, Z., Sun, P., Huang, T., Xue, J., Lee, J.W., Zhu, C., et al. (2018). Tailored Phase Conversion under Conjugated Polymer Enables Thermally Stable Perovskite Solar Cells with Efficiency Exceeding 21. J. Am. Chem. Soc. *140*, 17255–17262.

50. Zheng, X., Lei, H., Yang, G., Ke, W., Chen, Z., Chen, C., Ma, J., Guo, Q., Yao, F., Zhang, Q., et al. (2017). Enhancing Efficiency and Stability of Perovskite Solar Cells via A High Mobility P-Type PbS Buffer Layer. Nano Energy *38*, 1–11.